Global Environmental Change 72 (2022) 102441

Contents lists available at ScienceDirect

Global Environmental Change

journal homepage: www.elsevier.com/locate/gloenvcha

Global long-term mapping of surface temperature shows intensified intra-city urban heat island extremes

Lorenzo Mentaschi [a,b,*], Grégory Duveiller [b,c], Grazia Zulian [b], Christina Corbane [b], Martino Pesaresi [b], Joachim Maes [b], Alessandro Stocchino [d], Luc Feyen [b]

[a] Department of Physics and Astronomy "Augusto Righi" (DIFA), University of Bologna, Bologna 40127, Italy
[b] Joint Research Centre (JRC), European Commission, Ispra, Italy
[c] Max Planck Institute for Biogeochemistry, Jena, Germany
[d] Department of Civil and Environmental Engineering, The Hong Kong Polytechnic University, Hong Kong, China

ARTICLE INFO

Keywords:
Urban Heat Island
SUHI
Global scale
Long-term
High space–time resolution
Extremes
Trends

ABSTRACT

Surface temperatures are generally higher in cities than in rural surroundings. This phenomenon, known as Surface Urban Heat Island (SUHI), increases the risk of heat-related human illnesses and mortality. Past global studies analysed this phenomenon aggregated at city scale or over seasonal and annual time periods, while human impacts strongly depend on shorter term heat stress experienced locally. Here we develop a global long-term high-resolution dataset of daytime SUHI, offering an insight into the space–time variability of the urban–rural temperature differences which is unprecedented at global scale. Our results show that across urban areas worldwide over the period 2003–2020, 3-day SUHI extremes are on average more than twice as high as the warm-season median SUHI, with local exceedances up to 10 K. Over this period, SUHI extremes have increased more rapidly than warm-season medians, and averaged worldwide are now 1.04 K or 31% higher compared to 2003. This can be linked with increasing urbanisation, more frequent heatwaves, and greening of the earth, processes that are all expected to continue in the coming decades. Within many cities there are hotspots where extreme SUHI intensity is 10–15 K higher compared to relatively cooler city parts. Given the limited human adaptability to heat stress, our results advocate for mitigation strategies targeted at reducing SUHI extremes in the most vulnerable and exposed city neighbourhoods.

1. Introduction

Nowadays, more than half of the human population lives in cities and in the foreseeable future most population growth will be in urban areas (United Nations, Department of Economic and Social Affairs, 2018). A prominent feature of cities' climate is the Urban Heat Island (UHI), whereby the temperature of urbanized areas noticeably differs from that of rural neighbouring zones (Arnfield, 2003; Oke, 1982), and is generally higher, especially in temperate climates when the surroundings are covered by dense vegetation (Zhao et al., 2014; Zhou et al., 2019). This phenomenon represents a hazard, as it exacerbates the effect of heat waves in cities (Marcotullio et al., 2021), with a consequent increase of the risk to human health (Heaviside et al., 2017; Sera et al., 2019; Sherwood and Huber, 2010).

The intensity of UHI as estimated from Land Surface Temperature (LST) is usually referred to as Surface Urban Heat Island (SUHI), and has been studied at different space/time scales by several authors. Peng et al. (2012) published a global estimation of SUHI based on 6 years of MODIS, finding significant correlations with variables such as the albedo of building materials and the concentration of vegetation. Clinton and Gong (2013) showed that sign and intensity of the heat island depends not only on the characteristics of the city, but also on the physical properties of the surrounding soil. Manoli et al. (2019), based on 1-year MODIS observations (CIESIN, 2016), underlined the heterogeneity, non-linearity of the link with processes such as precipitation and surrounding temperature. Chakraborty and Lee (2019) analyzed the UHI globally on the whole extent of the MODIS mission (2003–2019), providing insight on the seasonal variability of SUHI and of its trends. Their analysis was further refined for the United States (Chakraborty et al., 2020). Ulpiani (2021) studied the link between UHI and pollution using data from 16 countries worldwide. UHI has been studied also in relation to climate change, with the development of projections (Zhao et al., 2021), and

* Corresponding author at: Department of Physics and Astronomy Augusto Righi, University of Bologna, Bologna, Italy.
E-mail address: lorenzo.mentaschi@unibo.it (L. Mentaschi).

https://doi.org/10.1016/j.gloenvcha.2021.102441
Received 23 April 2021; Received in revised form 14 November 2021; Accepted 29 November 2021

large-scale assessment of city policies (Estrada et al., 2017). These studies shed light on the global phenomenology of UHI, however, they focus primarily on coarse-grained representations of UHIs, where the thermal behaviour is lumped spatially over urban centres (Ajaaj et al., 2018; Varquez and Kanda, 2018) and temporally over seasonal (Chakraborty and Lee, 2019; Manoli et al., 2019) or annual (Peng et al., 2012) time scales. As a consequence, they fail to capture UHI peaks that are localised in space and time, and that are better represented in local, fine-scale studies (e.g. Armson et al., 2012; Tzavali et al., 2015; Wang et al., 2019b). Characterising temporal fluctuations is of foremost importance to assess the real threat posed to human health by urban heat, as phenomena such as heat waves can often last only few days (Gao et al., 2015; Meehl and Tebaldi, 2004; Nitschke et al., 2007; Zhao et al., 2018). Moreover, UHI intensity can vary between different parts of the same city (Masson et al., 2020) depending on their morphology and on the thermodynamic proprieties of their constitutive elements (e.g. densely built-up areas vs green areas). Finally, spatial averaging can dilute the intensity of the hazard felt locally.

A large number of small/medium-scale studies also exist, based on both remote and in-situ observations, which are better able to capture the fine-grained space–time variability of UHI (e.g. Dousset et al., 2011; Marando et al., 2019; Tan et al., 2010; Ward et al., 2016 and many others). Such studies can be precious tools for local assessments of the risk related to urban heat. However, they are often performed on time-limited and not always representative empirical cases, and employ different types of measurements and methodologies. Therefore, it is difficult to intercompare their results and reach general quantitative conclusions on causal relationships (Masson et al., 2020). Moreover, they cover extensively a few developed areas, such as Northern America, Europe and Eastern Asia, leading to a knowledge gap with respect to less studied regions (Mabon and Shih, 2021).

To fill these gaps, here we estimate daytime SUHI as the difference in LST between urban pixels and their rural surroundings at 1×1 km globally with a daily time step for the period 2003–2020. We use LST retrieved from satellite observations of the MODIS Aqua mission and built-up surfaces of the Global Human Settlements Layer (GHSL) (Corbane et al., 2020) to delineate urban pixels. We focus our analysis on the warm season, when urban heat is more likely to represent a risk to human health (Clinton and Gong, 2013; Peng et al., 2012; Zhou et al., 2014). As the highest effects on people typically appear within 3 days of extreme heat event onset (Gao et al., 2015) we put emphasis on 3-day (consecutive) averaged values of SUHI. We present a global picture of short-term SUHI extremes and assess how they compare with seasonal average values. We further quantify the temporal dynamics in SUHI extremes since 2003.

2. Material and methods

2.1. Mapping land surface temperature and built-up surfaces

Daily data of Land Surface Temperature (*LST*) were taken from the MODIS Aqua product of global Land Surface Temperature/Emissivity (MYD11A1 version 6, Wan and Li, 2011) for the period from January 2003 until December 2020. This 1-km resolution dataset was chosen for its quasi-daily coverage of the world surface. The satellite Aqua was preferred to Terra because it provides measurements in the early afternoon, approximately at the time of highest solar radiation and maximum daily surface temperature. The MYD11A1 data product was preferred over the more recent MODIS Aqua MxD21 LST product (MYD21A1, Hu et al., 2019) as it is less affected by noise, and provides more conservative estimations of temperature maxima and trends (Yao et al., 2020).

The extent of built-up surfaces used to define urban and non-urban areas has been mapped by means of satellite imagery classification. We used the most recent version of the Global Human Settlement Layer (GHSL, Corbane et al., 2020), based on Sentinel-2. It is based on convolution neural network modelling for pixel-wise image classification of built-up areas and provides at 10-m resolution the probability (between 0 and 100%) of a pixel to belong to the class built-up for the year 2018, as estimated by the classification algorithm.

There exist alternative datasets of urban mapping to GHSL (e.g. Marconcini et al., 2020), while also global imperviousness datasets are available (e.g. Gong et al., 2020; Huang et al., 2021a; Huang et al., 2021b; Yang et al., 2021). While impervious surface is strongly related to built-up surface, confusion can exist between bare soil and impervious areas (not including buildings with roof tops), which could distort the estimation of SUHI, especially in dry areas. Furthermore, the high resolution of Sentinel 2 (10 m) allows for a more accurate mapping of both built-up and impervious areas (Xu et al., 2018). Overall, the GHSL layer was chosen as a state-of-the-art, high-resolution dataset able to reliably capture built-up features at 10 resolution pixel level, even in areas of low-building density, and for a recent year (2018).

The handling of the large datasets and the analysis of SUHI as described below was carried out on the Google Earth Engine (Gorelick et al., 2017).

2.2. Estimation of SUHI

SUHI is defined as the difference in LST between urban and non-urban or rural areas. The term rural, which acquires distinct semantics in different literary contexts, is broadly used in scientific literature to indicate any type of non-urban territory (Hart et al., 2005). Here it identifies any pixel that is not built-up. The resolution of the built-up information from GHSL (10 m) is higher than that of the LST from MODIS (1 km). For each MODIS 1-km pixel the mean built-up probability was estimated for the year 2018 by averaging the probability values of the 10-m GHSL pixels contained inside of it. Then, MODIS pixels with a mean probability $> 15\%$ were considered as built-up. The choice of this threshold originates from the analysis by Corbane et al. (2020) on 277 areas of interest. Their results suggest that for the generation of a global binary classification from the probabilistic output of the models, a low probability threshold is recommended, especially if the purpose is to capture all the scattered settlements in rural landscapes. In particular, a 20% cut-off is indicated as threshold to classify low-density settlements with reasonable accuracy. However, in a few cases, characterized by very low building density, using even lower thresholds (15%) is preferable. Our choice is further justified by the fact that our objective is the exclusion of built-up pixels from the computation of the surrounding non-urban temperature.

It is worth noting, that our pixelwise definition of SUHI is based on a distinction between built-up pixels and neighbouring rural areas, rather than on a definition of city boundaries as usually done in studies on Urban Heat Island. As a result, the estimations of SUHI at any built-up pixel are valid through the whole 18-year of observations, as long as its temperatures are compared with the ones of persistently rural zones. Thus, the choice of a single, recent layer of urbanization does not represent a limitation under the assumption that pixels that were rural in 2018 were rural also earlier (i.e. neglecting de-urbanizing trends). On the other hand, using a recent year as a reference comes with advantages, as it provides a consistent way to appreciate the long-term evolution of areas characterized by intense urbanizing trends. Our methodology is consistent with earlier studies, which found large biases in the values of SUHI estimated from outdated urban maps (Zhao et al., 2016). And in this respect, a limitation is that in the selection of built-up and rural pixels we neglect the urbanization ongoing after 2018.

Although water bodies can dampen SUHI in nearby and downwind locations, they should be excluded from the surrounding rural area considered in the calculation of SUHI, as that would artificially inflate SUHI values. For the detection of water bodies, we used the Global Surface Water (GSW) dataset (Pekel et al., 2016) available at 30-m resolution. For each MODIS pixel, the percentage of surface occupied by water was estimated from GSW, and 1-km pixels with water presence $>15\%$ were excluded from the computation. The latest available raster

of water presence was employed (year 2019).

The intensity of the SUHI was estimated from LST by means of a kernel-based approach whereby the same procedure was applied to all the urban pixels of all the imagery available in MYD11A1. For each 1-km built-up pixel the LST was obtained directly from MODIS and is denoted by $LST_{built\text{-}up}$. The corresponding value for the rural surroundings (LST_{rural}), was computed as the median LST of all non-built-up non-water pixels within a kernel consisting of a 70 km-side square centred on the built-up pixel. This size guarantees that in the majority of the cities, for any built-up pixel there are at least 500 non-built-up pixels for the computation of LST_{rural}. The only city where this condition is violated in a part of the urban area is Shanghai, for which a double-size kernel (a 140 km-side square) was used. The SUHI was then computed pixelwise as the difference between the *LST* of the built-up pixel ($LST_{built\text{-}up}$) and the surrounding non-urban area (LST_{rural}):

$$SUHI = LST_{built-up} - LST_{rural} \quad (1)$$

The quality of LST was assessed prior to the computation of SUHI. In particular:

- MYD11A1 provides estimates of LST only for pixels in clear sky conditions with a confidence of at least 95% (Wan, 2013).
- For LST_{rural} only estimates with average error < 1 K were considered.
- For LST_{urban} only estimates with average error < 2 K were considered.
- An estimate of SUHI was considered unreliable if <20% of the non-urban pixels was in clear-sky conditions.

Elevation is an important factor that influences LST and placing urban and rural pixels at similar elevation is required to isolate the effect of urbanisation on SUHI (Stewart, 2011). Previous studies tackled this problem by considering only urban and non-urban pixels approximately at the same altitude (e.g. Chakraborty and Lee, 2019). However, in some cases this approach limits considerably the availability of non-urban pixels for the computation of LST_{rural}. Here we opted for an altitude-based correction of LST prior to comparing the values at different pixels. In particular, LST was corrected to the mean altitude of the 70 km-size square centred in the pixel (140 km in proximity of Shanghai) by considering an Environmental Lapse Rate (ELR) of −6.5 K per 1000 m of altitude (Hartmann, 2015). Though such value can be subject to significant local variability (e.g. Firozjaei et al., 2020), it is often used as a reference in studies on near-surface temperature (e.g. Sospedra-Alfonso et al., 2015) and LST (e.g. Deng et al., 2018; Jain et al., 2008). Given the lack of global studies on the topic, and the significant uncertainty that often characterizes local estimations of ELR (Lute and Abatzoglou, 2021), this order-of-magnitude correction represents the best that can be done at present. To account for the effects of surface relief we used the Shuttle Radar Topography Mission data provided by the U.S. Geological Survey (USGS, 2009) at 100-m resolution.

The kernel-based approach used in this study comes with advantages with respect to techniques relying on a definition of urban area based on population or other socioeconomic indicators, in terms of robustness and reproducibility. It has only 2 degrees of freedom: the cut-off to define the built-up pixels (15% of built-up probability), and the kernel size (70 km, everywhere with the exception of Shanghai where the kernel size is 140 km). Furthermore, its application to all the built-up pixels, including the ones not located in urban areas delineated on the basis of socioeconomic indicators, enables the possible future study of the urban-non urban continuum.

2.3. SUHI in Functional urban areas

Though the estimation of SUHI was carried out and stored for all built-up 1-km pixels worldwide, we report spatial and temporal statistics over built-up pixels enclosed within the spatial boundaries of 9028 Functional Urban Areas (FUA, Schiavina et al., 2019). FUAs consist of high-density urban centres with at least 50 thousand people together with their surrounding commuting zones (Dijkstra et al., 2019). Nowadays, 53% of the world population (3.9 billion people) live inside FUAs (Moreno-Monroy et al., 2020). They are used here to identify urban contexts, leaving out small and isolated extra-urban centres made up of few built-up pixels. Overall, >1,200,000 1-km urban pixels (i.e. built-up pixels located in a FUA) where considered in the discussion.

2.4. SUHI during the warm season

The analysis presented in this manuscript focuses on SUHI during the warm season, when human heat stress is typically the highest (Clinton and Gong, 2013; Peng et al., 2012; Zhou et al., 2014). Past studies used a temperate-zone definition of summer, i.e., the months of June, July, August (JJA) for the Northern Hemisphere (NH), the months of December, January, February (DJF) for the Southern Hemisphere (SH) (e.g. Chakraborty and Lee, 2019; Manoli et al., 2019; Peng et al., 2012; Zhou et al., 2017). However, in some tropical and subtropical areas, these months may partially coincide with the raining season (Dash et al., 2009; Nicholson et al., 2000; Song et al., 2011). This reduces the likelihood of intense heatwaves and the number of reliable observations of SUHI. Therefore, we defined the warm season as:

- For temperate and polar regions (latitude above 35°N/S), the months of JJA/DJF in the NH/SH.
- For tropical and subtropical regions (10°N/S < latitude < 35°N/S), the months of April, May, June, July, August, September (AMJJAS) in the NH, the months of October, November, December, January, February, March (ONDJFM) in the SH.
- For areas closer than 10° to the equator, characterized by persistent warm conditions, the whole year was considered.

This definition of warm season comes with the availability in tropical and equatorial areas of a significantly larger sample of data, compared with the usual 3-months warm season (Fig. S1), resulting in more reliable statistics in many areas frequently cloud-covered.

Human impacts of heat are highest when conditions of high temperature last for several days (Gao et al., 2015; Meehl and Tebaldi, 2004; Nitschke et al., 2007). In each urban pixel the daily estimates of SUHI during the warm season were therefore temporally aggregated by means of a 3-day moving average, requiring the presence of valid estimates of SUHI in each of 3 consecutive days. From the resulting time-averaged time series, we estimated the following statistics for each urban pixel: (1) the warm-season medians ($SUHI_{seas}$), which represents a central estimate of the SUHI in the warm season for each year between 2003 and 2020; (2) the 1-year maxima ($SUHI_{1y}$), which represents the maximum 3-day SUHI in the warm season for each year between 2003 and 2020; and (3) the 18-year maximum ($SUHI_{18y}$), which represents the maximum 3-day SUHI estimated over all the warm seasons between 2003 and 2020. The space–time statistics (medians, 95th percentiles, maxima, % above zero) of $SUHI_{seas}$, $SUHI_{1y}$, shown in Table 1, were estimated by computing a pixelwise median between the annual values, and then considering the resulting spatial distribution. For $SUHI_{18y}$, which is not defined along a time axis, the statistics were estimated directly from the spatial raster.

Trends were estimated on the annual values of $SUHI_{1y}$ and $SUHI_{seas}$ for the world and 11 macro-regions (Europe, Middle East + North Africa, Sub-Saharan Africa, Russia + Ukraine + Commonwealth of Independent States (CIS), East Asia, South Asia, Southeast Asia, Oceania, North America, Central America, and South America, Fig. S2. $SUHI_{1y}$ and $SUHI_{seas}$ estimates at pixel level were first aggregated to macro-region by taking the spatial median over urban pixels in FUA of the considered macro-region. The trend's slope was then estimated on the macro-region annual $SUHI_{1y}$ and $SUHI_{seas}$ values using a Theil-Sen estimator (Theil, 1992). In the computation of the trends, all the built-

Table 1
Quantities examined in this study ($SUHI_{18y}$, $SUHI_{1y}$, $SUHI_{seas}$, and the differences $SUHI_{18y} - SUHI_{seas}$ and $SUHI_{1y} - SUHI_{seas}$) and their definitions, and space–time statistics: median, 95th percentile, maxima, % below 0. The figures for $SUHI_{18y}$ are computed from the global spatial distribution of urban pixels. The figures for $SUHI_{1y}$ and $SUHI_{seas}$ are computed by performing a median on the annual values and then considering the resulting global spatial distribution.

Quantity	Definition	median (K)	95th perc. (K)	max (K)	% below 0
$SUHI_{18y}$	18-year warm-season maximum of the 3-day moving average of daytime SUHI	5.9	11.3	>16	2.3
$SUHI_{1y}$	1-year warm-season maximum of the 3-day moving average of daytime SUHI	4.0	9.1	>13	7.0
$SUHI_{seas}$	Warm-season median of the 3-day moving average of daytime SUHI	2.5	7.3	>12	18.0
$SUHI_{18y} - SUHI_{seas}$	Pixel-wise difference between 18-year maximum and warm-season median	3.3	6.9	>12	–
$SUHI_{1y} - SUHI_{seas}$	Pixel-wise Difference between 1-year maximum and warm-season median	1.4	4.2	>7	–

up pixels estimated from GHSL for the year 2018 and contained in the FUAs were considered. Hence, the obtained trend accounts for urbanization whereby pixels that in the past were rural underwent a process of progressive urbanization, thus developing the onset of the SUHI phenomenon.

3. Results and discussion

3.1. Short-term maxima versus temporally aggregated SUHI

Across all urban areas worldwide over the period 2003–2020, the space–time median $SUHI_{seas}$ is 2.5 K (Fig. 1 and Table 1). This corroborates earlier global (Clinton and Gong, 2013; Peng et al., 2012) and regional (Zhou et al., 2019) studies that report annually and seasonally averaged SUHI intensities of few degrees. Short-term maxima are significantly higher, with a global 18-year space–time median $SUHI_{1y}$ of 4.0 K, annual 3-day peaks of SUHI are on average 1.5 K more intense than the seasonal SUHI. Under extreme conditions of urban surface warming, represented by $SUHI_{18y}$, this rises to nearly 6.0 K, or more than a doubling of the seasonal SUHI intensities.

There is large variation around the central global estimates. Extreme SUHI intensity ($SUHI_{18y}$) can reach beyond 16 K, with a global 95th percentile of 11.3 K. This is about 4 K higher than the corresponding statistics for the warm-season median SUHI ($SUHI_{seas}$). At pixel level, $SUHI_{1y}$ exceeds $SUHI_{seas}$ by a maximum of > 7 K, and by 4.2 K in 5% of urban pixels. For $SUHI_{18y}$, the pixel-wise differences with $SUHI_{seas}$ are even larger and reach 6.9 K in 5% of urban pixels, with a maximum difference >12 K. While synergies between heat waves and SUHI have not been fully understood and remain subject of debate (Scott et al., 2018), several studies have shown amplified urban warming under heat waves, especially in temperate regions (Zhao et al., 2018). Hence, during times when background heat is most pronounced, strongly intensified SUHI can considerably add to the heat stress in cities.

Eighteen percent of urban pixels present negative values of $SUHI_{seas}$, whilst this fraction is much reduced if maxima are considered: $SUHI_{1y}$ is negative in 7% of the pixels and $SUHI_{18y}$ is negative in 2.3% of the pixels. This suggests that cities, or parts thereof, that generally act as heat sinks (i.e., urban areas cooler than their surroundings, Clinton and Gong, 2013) may occasionally behave as heat islands (Fig. S3).

The global map of $SUHI_{18y}$ (Fig. 1f) shows strong spatial heterogeneity in extreme surface urban warming, but some geographic patterns can be observed linked with background climate. $SUHI_{18y}$ is generally higher at mid-high latitudes in areas characterized by temperate and humid conditions, where dense and aerodynamically rough vegetation in rural areas results in higher evapotranspiration rates and convection efficiency compared to their urban counterparts. In drier regions, evapotranspiration and convection efficiency of low stature natural vegetation outside cities is lower, resulting in smaller or even negative values of UHI, possibly intensified by the presence of urban vegetation (Manoli et al., 2019; Zhao et al., 2014). Monsoon and equatorial regions also show mostly milder $SUHI_{18y}$ intensities, which relates to a levelling of the precipitation effect on evapotranspiration above 1500 mm yr^{-1} and decreasing urban warming intensities for warmer climates (Chow and Roth, 2006; Manoli et al., 2019). Apart from the considerably higher values found for $SUHI_{18y}$ compared to $SUHI_{seas}$, the large-scale patterns in $SUHI_{18y}$ are in general consistent with those observed for $SUHI_{seas}$ (see Fig. S4a) and found in earlier studies for city-scale seasonal means (Chakraborty and Lee, 2019; Manoli et al., 2019; Peng et al., 2012). We notice that areas characterized by strong climatic variability during the warm season, e.g. monsoon regions, usually experience a stronger difference between seasonal averages and maxima (Fig. S4b,c) that can be linked to more distinctive seasonal hysteretic cycles of urban and rural temperatures (Manoli et al., 2020).

3.2. Long-term trends in SUHI maxima

We find that across all urban centres worldwide SUHI maxima ($SUHI_{1y}$) have increased on average by nearly 1.04 K, or 0.06 K yr^{-1}, between 2003 and 2020 (Fig. 2). Eastern Asia shows the strongest rise of 0.12 K yr^{-1}, which can be linked to the rapid urbanisation in the region (United Nations, Department of Economic and Social Affairs, 2018). This is exemplified by the city of Tianjin, where the urban area nearly quadrupled between 1980 and 2010 (Wu et al., 2015) and the trend in $SUHI_{1y}$ locally exceeds 0.3 K yr^{-1} (Fig. 2n). Despite the general trend of urbanisation and consequent urban warming in the region (Yang et al., 2019), some cities in Eastern Asia show distinctive signs of declining population in inner-city areas (Liu et al., 2020). This can cause a downward trend in SUHI in shrinking city parts, such as in Seoul, where after 2000 the population decline and renewal of the central business district led to reduced UHI intensities in the city centre (Hong et al., 2019, Fig. 2m. While the process of city shrinking is emerging in Asian cities, it has been observed for many decades in US and Europe (Martinez-Fernandez et al., 2016), and even in developing countries a number of large cities have been affected by this phenomenon (State of the world's cities 2008/2009: *Harmonious cities*, 2012). In many cases this is accompanied by suburbanisation, which shifts the burden to newly built-up suburbs where extreme SUHI can rise rapidly.

It is worth remarking that our pixelwise methodology is capable to fully capture the tendencies of SUHI in different contexts, and to provide stake holders and administrators with information which clearly relates to ongoing local environmental changes and/or urban policies. For example, in areas which underwent urban renewal, such as the central business district of Seoul, where the trend is prevalently negative. As well as in neighbourhoods which were rural or sparsely built-up in 2003, and saw an intense process of urbanization in the last 2 decades, such as the peripheries of Seoul and Tianjin, where the values of SUHI increased from near zero to those typical of a fully developed urban heat island.

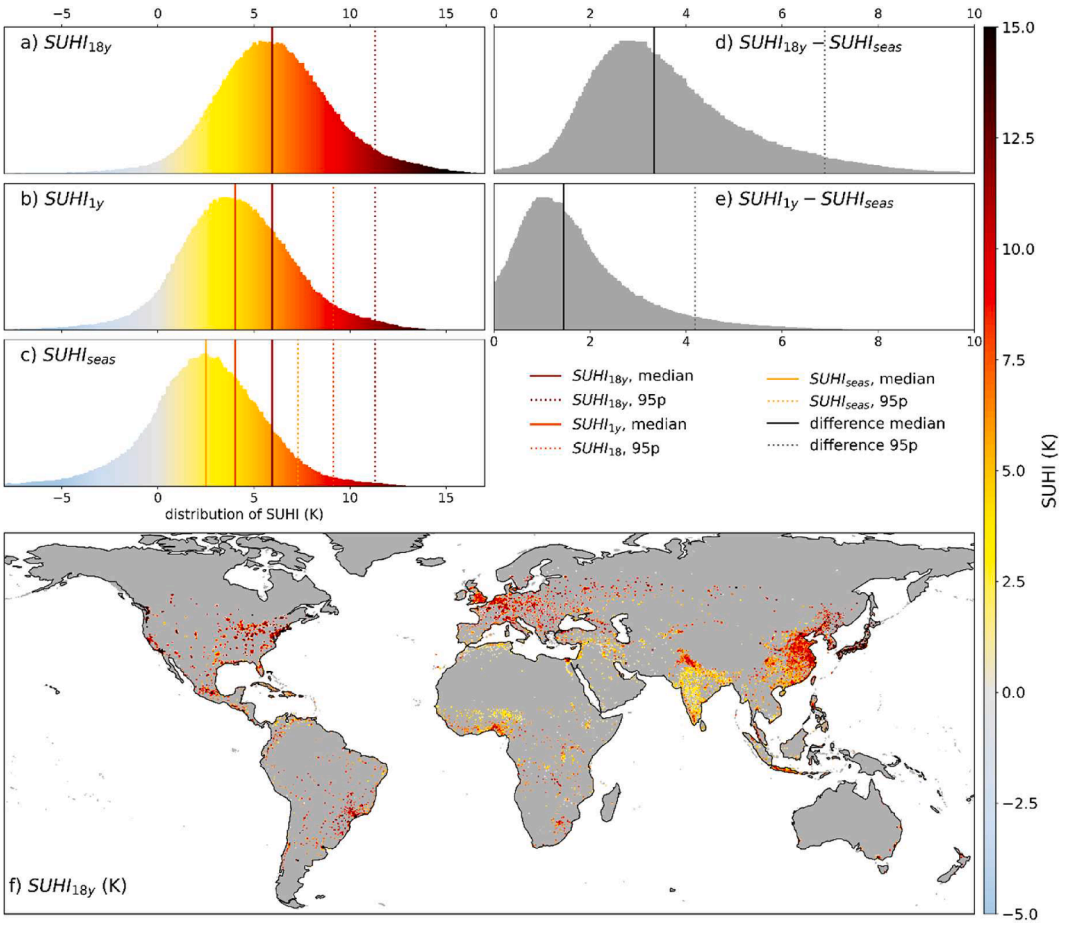

Fig. 1. Global distribution of warm-season SUHI indices. a, Histogram across urban pixels worldwide of the pixel warm-season 3-day SUHI maximum over the 18 years analysed ($SUHI_{18y}$). b, Histogram across all urban pixels worldwide of the pixel median of the yearly warm-season 3-day SUHI maxima ($SUHI_{1y}$) of the 18 years analysed. c, Histogram across all urban pixels worldwide of the pixel warm-season SUHI median ($SUHI_{seas}$) over the 18 years analysed. d, Histogram across all urban pixels worldwide of the pixel difference between $SUHI_{18y}$ and the 18-year median $SUHI_{seas}$. e, Histogram across all urban pixels worldwide of the pixel difference between $SUHI_{1y}$ and the 18-year median $SUHI_{seas}$. The solid and dashed vertical lines in the histograms in a-e represent the median and 95th percentile over all urban pixels worldwide for the respective indices and differences therein. f, Global map of warm-season 3-day SUHI maximum over the 18 years analysed ($SUHI_{18y}$) in urban pixels. Urban pixels are defined as 1 × 1 km built-up pixels enclosed within the spatial boundaries of Functional Urban Areas (FUA). FUA are cities and their surroundings and nearly four billion people live in the 9028 FUAs worldwide.

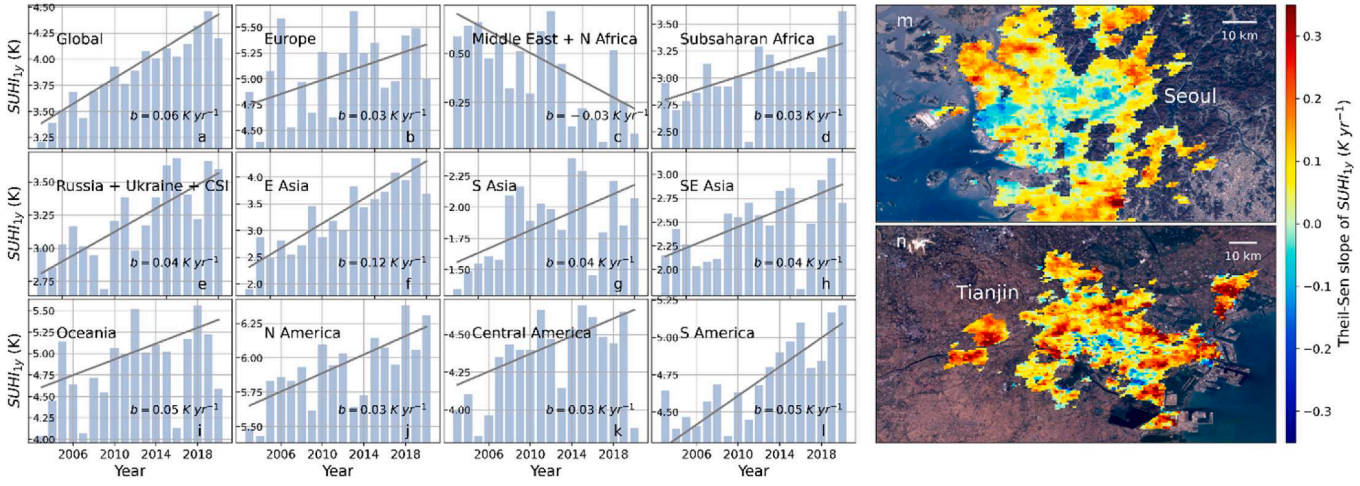

Fig. 2. Trend in yearly SUHI maxima of the warm season. Trend of $SUHI_{1y}$ for the globe (a) and in different macro-regions (b-l). In each panel the Theil-Sen slope (Gong et al., 2020) is reported (coefficient b). For the globe and all macro-regions the slope is significant beyond the 95% confidence. m-n, Maps of the trend (in K yr^{-1}) in Seoul (m) and Tianjin (n). Fig. S6 shows the pixels built-up between 2000 and 2015 according to GHSL.

Despite the strong urbanisation in Southern and South Eastern Asia, but also in sub-Saharan Africa (United Nations, Department of Economic and Social Affairs, 2018), the rate of increase in extreme daytime UHI intensity is two to four times lower compared to Eastern Asia. This is consistent with the fact that SUHI is generally less intense in arid and tropical regions than in temperate ones. In the very hot and dry climate of the Middle East and North Africa the trend is negative as urbanisation generally results in heat sinks.

Extreme urban surface warming has increased less strongly also in North America (0.03 K yr^{-1}), Europe (0.03 K yr^{-1}), South-America (0.05 K yr^{-1}), and Oceania (0.05 K yr^{-1}). With already >70% of population living in urban centres in these regions (Carneiro Freire et al., 2019), urbanisation in recent decades has been lower compared to strongly developing areas. However, at present these regions still show the highest extreme SUHI intensities, with average $SUHI_{1y}$ above 6 K for cities in North-America, close to 5.5 K in Oceania and Europe, and around 5 K in South-America.

Extreme SUHI intensities show in general a stronger increasing trend in time compared to median warm-season values (Fig. S5), but there are strong geographic differences. In South-America, $SUHI_{1y}$ has increased by 0.05 K yr^{-1} compared to 0.02 K yr^{-1} for $SUHI_{seas}$, implying extreme urban surface warming has increased more than double the rate of the seasonal values. Also in Europe and Russia extreme SUHI intensities have clearly risen more. In sub-Saharan Africa there is no trend in $SUHI_{seas}$ while $SUHI_{1y}$ has increased by nearly 0.5 K between 2003 and 2020. In South Asia, $SUHI_{seas}$ has become slightly less negative, while $SUHI_{1y}$ increased from 1.4 K to nearly 2 K on average over the region (Fig. 2).

A generally upward trend in temporally-aggregated urban warming has been reported before, with strong variations between cities (Ajaaj et al., 2018; Varquez and Kanda, 2018). This is driven by the continued urbanisation around the world (Gong et al., 2020; United Nations, Department of Economic and Social Affairs, 2018), the greening of natural vegetation (Yao et al., 2019) and cropland (Chen et al., 2019) in rural areas, and modulated by background climate (Manoli et al., 2019; Zhao et al., 2014) and artificial dynamics (Hong et al., 2019; Nichol et al., 2020). The more pronounced trend in $SUHI_{1y}$ compared to $SUHI_{seas}$ suggests a higher sensitivity of extreme SUHI to urbanisation. Current understanding does not indicate that global warming directly enhances differences in rural–urban warming (Masson et al., 2020), but the observed increase in heatwave days almost everywhere since the 1950s (Perkins-Kirkpatrick and Lewis, 2020) and possible synergies between heat waves and SUHI (Zhao et al., 2018) can partially explain the stronger increase in SUHI extremes. The amplification of greenness-climate feedbacks during extreme climate conditions (Forzieri et al., 2017) further suggests stronger positive effects of greening of non-urban areas on extreme SUHI compared to temporally-aggregated urban warming.

3.3. A zoom on city scale variability

Our global dataset allows to explore at an unprecedented level of detail the local space–time features of SUHI in all the worlds' cities, which until now have been appreciated only in local studies. A zoom on 14 megacities spread over the different continents reveals highly diversified intra-city pictures of extreme surface urban warming (Fig. 3). Across these urban centres, $SUHI_{18y}$ varies on average by 12.8 K (Fig. 3, Table 1), with the highest spatial variability observed in Tokyo ($0.9 \leq SUHI_{18y} \geq 17.6$ K) and New York ($0.1 \leq SUHI_{18y} \geq 16$ K), and the lowest in Paris ($2.1 \leq SUHI_{18y} \geq 12.7$ K) and London ($0.8 \leq SUHI_{18y} \geq 10$ K).

While each city has its own unique combination of climate, geography, and internal structure, some common patterns can be observed. Hotspots are often found in industrial parts of cities, where waste heat, the use of dark construction material and absence of vegetation can result in high SUHI intensities (Portela et al., 2020). For example, in New York particularly high values of $SUHI_{18y}$ can be observed South of Newark, where the international airport, a railroad and other industrial facilities are located (Fig. S7). In Paris the hotspots of $SUHI_{18y}$ are east of Saint-Denise and near Chevilly Larue, both areas with large industrial complexes (Fig. S8). Similar examples can be found for all of the examined cities (Fig. 2).

In Mexico City high values of $SUHI_{18y}$ can be found in areas characterised by a high concentration of slums, such as Ciudad Nezahualcoyotl and Iztapalapa (Fig. S9). This corroborates the link between the chaotic, dense and unregulated urbanisation typical of slums and intense heat exposure (Wang et al., 2019a). Combined with poverty, poor housing conditions and little access to cooling options this poses serious health threats to people (Teare et al., 2020).

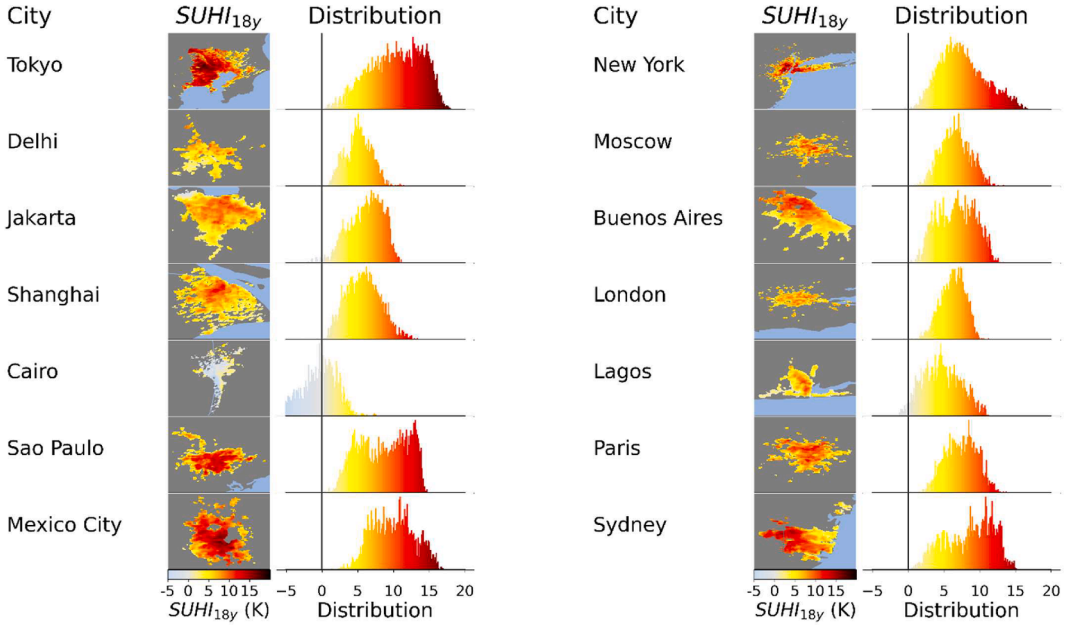

Fig. 3. Distribution of warm-season extreme SUHI in megacities. Maps (left panels) and histograms (right panels) of warm-season 3-day SUHI maximum over the 18 years analysed ($SUHI_{18y}$). Considered are all urban pixels within the Functional Urban Areas for each of the 14 world megacities.

Urban parks and green zones often correspond to relatively cooler areas. This can be observed, for example, for the forest areas in Hachioji (Tran et al., 2006), at the Sayama lake, and in the Chiyoda park in Tokyo, the Bois de Boulogne and the Bois de Vincennes in Paris, Hampstead Heath in London, La Tourette Park in New York (Fig. S10, S8, S11, S6). Water bodies within the city can also dampen $SUHI_{18y}$ intensity, as exemplified by the River Thames in London (Fig. S11). These findings confirm the important role of urban green and water in the mitigation of SUHI (Weng et al., 2004). In coastal cities, proximity to the sea can mitigate $SUHI_{18y}$, as can be observed in Buenos Aires, Sydney and Jakarta, but sea breeze cooling effects can be inhibited by tall buildings on the seafront or inner city (Masson et al., 2020).

The low values of $SUHI_{18y}$ observed in Cairo are explained by the drier climate, with surrounding deserts that warm up fast in clear sky conditions, and scarce vegetation and evapotranspiration cooling. Partially located upstream of the Nile delta, the city lays in a more humid, vegetated area and even $SUHI_{18y}$ is low or negative (down to below −5 K).

4. Conclusions

The dataset developed in this study consists of a global, consistent, high space–time resolution estimation of SUHI, based on a pixelwise distinction among built-up and rural areas, and offers insight into the local variability and evolution of urban/rural temperature differences, which are not captured by previous global coarser-grained spatiotemporal representations of SUHI (e.g. Manoli et al., 2019; Peng et al., 2012).

Our results reveal that short-term (3-day) maxima of day SUHI can be several degrees higher than seasonally estimated SUHI, with differences up to 10 K and more, while they can vary by an order of magnitude within cities. While SUHI extremes are already intensifying, continued urbanisation (United Nations, Department of Economic and Social Affairs, 2018), a growing number of slum dwellers, and a further rise in the frequency and intensity of hot spells with global warming (Dosio et al., 2018; Russo et al., 2019; Zhao et al., 2020), could elevate urban heat stress and consequent health risk to unprecedented levels in the most exposed and vulnerable city neighbourhoods in the near future. The management of extreme heat in cities will therefore be a major challenge to improve health and the urban environment. Past studies highlighted the need of focusing on areas where urban heat stress has not been analysed extensively, in support of context-aware urban mitigation policies (Mabon and Shih, 2021). Global urban science can tackle such gap by building fine-grained UHI models applicable across urban settlements worldwide, including under-studied regions and smaller cities (Acuto, 2016; Romero-Lankao et al., 2012), in order to forge new knowledge on urban warming extremes and their drivers. The dataset produced in this study, available on the Google Earth Engine, offers this opportunity.

CRediT authorship contribution statement

Lorenzo Mentaschi: Conceptualization, Formal analysis, Investigation, Methodology, Software, Writing – original draft, Visualization, Resources, Data curation. **Grégory Duveiller:** Writing - review & editing. **Grazia Zulian:** Writing - review & editing. **Christina Corbane:** Resources, Data curation, Writing - review & editing. **Martino Pesaresi:** Resources, Data curation, Writing - review & editing. **Joachim Maes:** Writing - review & editing. **Alessandro Stocchino:** Writing - review & editing. **Luc Feyen:** Conceptualization, Formal analysis, Investigation, Writing - review & editing.

Declaration of Competing Interest

The authors declare that they have no known competing financial interests or personal relationships that could have appeared to influence the work reported in this paper.

Acknowledgment

The authors declare that they have no known competing financial interests or personal relationships that could have appeared to influence the work reported in this paper.

Appendix A. Supplementary data

Supplementary data to this article can be found online at https://doi.org/10.1016/j.gloenvcha.2021.102441.

References

Acuto, M., 2016. Give cities a seat at the top table. Nature. https://doi.org/10.1038/537611a.

Ajaaj, A.A., Mishra, A.K., Khan, A.A., 2018. Urban and peri-urban precipitation and air temperature trends in mega cities of the world using multiple trend analysis methods. Theor. Appl. Climatol. https://doi.org/10.1007/s00704-017-2096-7.

Armson, D., Stringer, P., Ennos, A.R., 2012. The effect of tree shade and grass on surface and globe temperatures in an urban area. Urban For. Urban Green. 11, 245–255. https://doi.org/10.1016/j.ufug.2012.05.002.

Arnfield, A.J., 2003. Two decades of urban climate research: a review of turbulence, exchanges of energy and water, and the urban heat island. Int. J. Climatol. 23, 1–26. https://doi.org/10.1002/joc.859.

Carneiro Freire, S.M., Corbane, C., Ehlrich, D., Florczyk, A., Kemper, T., Maffenini, L., Melchiorri, M., Pesaresi, M., Schiavina, M., Tommasi, P., 2019. Atlas of the Human Planet 2019. Bruxelles. https://doi.org/10.2760/014159.

Center for International Earth Science Information Network - CIESIN - Columbia University, 2016. Global Urban Heat Island (UHI) Data Set, 2013. Palisades. 10.7927/H4H70CRF.

Chakraborty, T., Hsu, A., Manya, D., Sheriff, G., 2020. A spatially explicit surface urban heat island database for the United States: characterization, uncertainties, and possible applications. ISPRS J. Photogramm. Remote Sens. 168, 74–88. https://doi.org/10.1016/j.isprsjprs.2020.07.021.

Chakraborty, T., Lee, X., 2019. A simplified urban-extent algorithm to characterize surface urban heat islands on a global scale and examine vegetation control on their spatiotemporal variability. Int. J. Appl. Earth Obs. Geoinf. 74, 269–280. https://doi.org/10.1016/j.jag.2018.09.015.

Chen, C., Park, T., Wang, X., Piao, S., Xu, B., Chaturvedi, R.K., Fuchs, R., Brovkin, V., Ciais, P., Fensholt, R., Tømmervik, H., Bala, G., Zhu, Z., Nemani, R.R., Myneni, R.B., 2019. China and India lead in greening of the world through land-use management. Nat. Sustainability 2, 122–129. https://doi.org/10.1038/s41893-019-0220-7.

Chow, W.T.L., Roth, M., 2006. Temporal dynamics of the urban heat island of Singapore. Int. J. Climatol. 26, 2243–2260. https://doi.org/10.1002/joc.1364.

Clinton, N., Gong, P., 2013. MODIS detected surface urban heat islands and sinks: Global locations and controls. Remote Sens. Environ. https://doi.org/10.1016/j.rse.2013.03.008.

Corbane, C., Syrris, V., Sabo, F., Politis, P., Melchiorri, M., Pesaresi, M., Soille, P., Kemper, T., 2020. Convolutional neural networks for global human settlements mapping from Sentinel-2 satellite imagery. Neural Comput. Appl. https://doi.org/10.1007/s00521-020-05449-7.

Dash, S.K., Kulkarni, M.A., Mohanty, U.C., Prasad, K., 2009. Changes in the characteristics of rain events in India. J. Geophys. Res. [Atmos.]. https://doi.org/10.1029/2008JD010572.

Deng, Y., Wang, S., Bai, X., Tian, Y., Wu, L., Xiao, J., Chen, F., Qian, Q., 2018. Relationship among land surface temperature and LUCC, NDVI in typical karst area. Sci. Rep. 8, 641. https://doi.org/10.1038/s41598-017-19088-x.

Dijkstra, L., Poelman, H., Veneri, P., 2019. The EU-OECD definition of a functional urban area. OECD Reg. Dev. Work. Pap. Éditions OCDE. https://doi.org/10.1787/d58cb34d-en.

Dosio, A., Mentaschi, L., Fischer, E.M., Wyser, K., 2018. Extreme heat waves under 1.5 °c and 2 °c global warming. Environ. Res. Lett. 13 https://doi.org/10.1088/1748-9326/aab827.

Dousset, B., Gourmelon, F., Laaidi, K., Zeghnoun, A., Giraudet, E., Bretin, P., Mauri, E., Vandentorren, S., 2011. Satellite monitoring of summer heat waves in the Paris metropolitan area. Int. J. Climatol. 31, 313–323. https://doi.org/10.1002/joc.2222.

Estrada, F., Botzen, W.J.W., Tol, R.S.J., 2017. A global economic assessment of city policies to reduce climate change impacts. Nat. Clim. Chang. 7, 403–406. https://doi.org/10.1038/nclimate3301.

Firozjaei, M.K., Fathololoumi, S., Alavipanah, S.K., Kiavarz, M., Vaezi, A.R., Biswas, A., 2020. A new approach for modeling near surface temperature lapse rate based on normalized land surface temperature data. Remote Sens. Environ. 242, 111746 https://doi.org/10.1016/j.rse.2020.111746.

Forzieri, G., Alkama, R., Miralles, D.G., Cescatti, A., 2017. Satellites reveal contrasting responses of regional climate to the widespread greening of Earth. Science 356, 1180–1184. https://doi.org/10.1126/science.aal1727.

Gao, J., Sun, Y., Liu, Q., Zhou, M., Lu, Y., Li, L., 2015. Impact of extreme high temperature on mortality and regional level definition of heat wave: a multi-city study in China. Sci. Total Environ. https://doi.org/10.1016/j.scitotenv.2014.10.028.
Gong, P., Li, X., Wang, J., Bai, Y., Chen, B., Hu, T., Liu, X., Xu, B., Yang, J., Zhang, W., Zhou, Y., 2020. Annual maps of global artificial impervious area (GAIA) between 1985 and 2018. Remote Sens. Environ. 236, 111510 https://doi.org/10.1016/j.rse.2019.111510.
Gorelick, N., Hancher, M., Dixon, M., Ilyushchenko, S., Thau, D., Moore, R., 2017. Google Earth Engine: Planetary-scale geospatial analysis for everyone. Remote Sens. Environ. 202, 18–27. https://doi.org/10.1016/j.rse.2017.06.031.
Hart, L.G., Larson, E.H., Lishner, D.M., 2005. Rural definitions for health policy and research. Am. J. Public Health 95, 1149–1155. https://doi.org/10.2105/AJPH.2004.042432.
Hartmann, D.L., 2015. In: Global Physical Climatology, second ed. https://doi.org/10.1016/C2009-0-00030-0
Heaviside, C., Macintyre, H., Vardoulakis, S., 2017. The Urban Heat Island: implications for health in a changing environment. Curr. Environ. Heal. Rep. 4, 296–305. https://doi.org/10.1007/s40572-017-0150-3.
Hong, J.-W., Hong, J., Kwon, E.E., Yoon, D.K., 2019. Temporal dynamics of urban heat island correlated with the socio-economic development over the past half-century in Seoul Korea. Environ. Pollut. 254, 112934 https://doi.org/10.1016/j.envpol.2019.07.102.
Hu, T., Li, H., Cao, B., van Dijk, A.I.J.M., Renzullo, L.J., Xu, Z., Zhou, J., Du, Y., Liu, Q., 2019. Influence of emissivity angular variation on land surface temperature retrieved using the generalized split-window algorithm. Int. J. Appl. Earth Obs. Geoinf. 82, 101917 https://doi.org/10.1016/j.jag.2019.101917.
Huang, X., Huang, J., Wen, D., Li, J., 2021a. An updated MODIS global urban extent product (MGUP) from 2001 to 2018 based on an automated mapping approach. Int. J. Appl. Earth Obs. Geoinf. 95, 102255 https://doi.org/10.1016/j.jag.2020.102255.
Huang, X., Li, J., Yang, J., Zhang, Z., Li, D., Liu, X., 2021b. 30 m global impervious surface area dynamics and urban expansion pattern observed by Landsat satellites: from 1972 to 2019. Sci. China Earth Sci. 64, 1922–1933. https://doi.org/10.1007/s11430-020-9797-9.
Jain, S.K., Goswami, A., Saraf, A.K., 2008. Determination of land surface temperature and its lapse rate in the Satluj River basin using NOAA data. Int. J. Remote Sens. 29, 3091–3103. https://doi.org/10.1080/01431160701468992.
Liu, Z., Liu, S., Song, Y., 2020. Understanding urban shrinkage in China: developing a multi-dimensional conceptual model and conducting empirical examination from 2000 to 2010. Habitat. Int. https://doi.org/10.1016/j.habitatint.2020.102256.
Lute, A.C., Abatzoglou, J.T., 2021. Best practices for estimating near-surface air temperature lapse rates. Int. J. Climatol. 41 https://doi.org/10.1002/joc.6668.
Mabon, L., Shih, W.-Y., 2021. Urban greenspace as a climate change adaptation strategy for subtropical Asian cities: a comparative study across cities in three countries. Glob. Environ. Chang. 68 https://doi.org/10.1016/j.gloenvcha.2021.102248.
Manoli, G., Fatichi, S., Bou-Zeid, E., Katul, G.G., 2020. Seasonal hysteresis of surface urban heat islands. Proc. Natl. Acad. Sci. 117, 7082–7089. https://doi.org/10.1073/pnas.1917554117.
Manoli, G., Fatichi, S., Schläpfer, M., Yu, K., Crowther, T.W., Meili, N., Burlando, P., Katul, G.G., Bou-Zeid, E., 2019. Magnitude of urban heat islands largely explained by climate and population. Nature. https://doi.org/10.1038/s41586-019-1512-9.
Marando, F., Salvatori, E., Sebastiani, A., Fusaro, L., Manes, F., 2019. Regulating Ecosystem Services and Green Infrastructure: assessment of Urban Heat Island effect mitigation in the municipality of Rome, Italy. Ecol. Modell. 392, 92–102. https://doi.org/10.1016/j.ecolmodel.2018.11.011.
Marconcini, M., Metz-Marconcini, A., Üreyen, S., Palacios-Lopez, D., Hanke, W., Bachofer, F., Zeidler, J., Esch, T., Gorelick, N., Kakarla, A., Paganini, M., Strano, E., 2020. Outlining where humans live, the World Settlement Footprint 2015. Sci. Data 7, 242. https://doi.org/10.1038/s41597-020-00580-5.
Marcotullio, P.J., Keßler, C., Fekete, B.M., 2021. The future urban heat-wave challenge in Africa: exploratory analysis. Glob. Environ. Chang. 66, 102190 https://doi.org/10.1016/j.gloenvcha.2020.102190.
Martinez-Fernandez, C., Weyman, T., Fol, S., Audirac, I., Cunningham-Sabot, E., Wiechmann, T., Yahagi, H., 2016. Shrinking cities in Australia, Japan, Europe and the USA: from a global process to local policy responses. Prog. Plann. https://doi.org/10.1016/j.progress.2014.10.001.
Masson, V., Lemonsu, A., Hidalgo, J., Voogt, J., 2020. Urban climates and climate change. Annu. Rev. Environ. Resour. 45, 411–444. https://doi.org/10.1146/annurev-environ-012320-083623.
Meehl, G.A., Tebaldi, C., 2004. More intense, more frequent, and longer lasting heat waves in the 21st century. Science. https://doi.org/10.1126/science.1098704.
Moreno-Monroy, A.I., Schiavina, M., Veneri, P., 2020. Metropolitan areas in the world. Delineation and population trends. J. Urban Econ. 103242 https://doi.org/10.1016/j.jue.2020.103242.
Nichol, J.E., Choi, S.Y., Wong, M.S., Abbas, S., 2020. Temperature change and urbanisation in a multi-nucleated megacity: China's Pearl River Delta. Urban Clim. 31, 100592 https://doi.org/10.1016/j.uclim.2020.100592.
Nicholson, S.E., Some, B., Kone, B., 2000. An analysis of recent rainfall conditions in West Africa, including the rainy seasons of the 1997 El Nino and the 1998 La Nina years. J. Clim. https://doi.org/10.1175/1520-0442(2000)013<2628:AAORRC>2.0.CO;2.
Nitschke, M., Tucker, G.R., Bi, P., 2007. Morbidity and mortality during heatwaves in metropolitan Adelaide. Med. J. Aust. https://doi.org/10.5694/j.1326-5377.2007.tb01466.x.
Oke, T.R., 1982. The energetic basis of the urban heat island. Q. J. R. Meteorol. Soc. https://doi.org/10.1002/qj.49710845502.
Pekel, J.-F., Cottam, A., Gorelick, N., Belward, A.S., 2016. High-resolution mapping of global surface water and its long-term changes. Nature 1–19. https://doi.org/10.1038/nature20584.
Peng, S., Piao, S., Ciais, P., Friedlingstein, P., Ottle, C., Bréon, F.M., Nan, H., Zhou, L., Myneni, R.B., 2012. Surface urban heat island across 419 global big cities. Environ. Sci. Technol. https://doi.org/10.1021/es2030438.
Perkins-Kirkpatrick, S.E., Lewis, S.C., 2020. Increasing trends in regional heatwaves. Nat. Commun. https://doi.org/10.1038/s41467-020-16970-7.
Portela, C.I., Massi, K.G., Rodrigues, T., Alcântara, E., 2020. Impact of urban and industrial features on land surface temperature: evidences from satellite thermal indices. Sustainable Cities Soc. https://doi.org/10.1016/j.scs.2020.102100.
Romero-Lankao, P., Qin, H., Dickinson, K., 2012. Urban vulnerability to temperature-related hazards: a meta-analysis and meta-knowledge approach. Glob. Environ. Chang. 22, 670–683. https://doi.org/10.1016/j.gloenvcha.2012.04.002.
Russo, S., Sillmann, J., Sippel, S., Barcikowska, M.J., Ghisetti, C., Smid, M., O'Neill, B., 2019. Half a degree and rapid socioeconomic development matter for heatwave risk. Nat. Commun. https://doi.org/10.1038/s41467-018-08070-4.
Schiavina, M., Moreno-monroy, A., Maffenini, L., Veneri, P., 2019. GHSL-OECD Functional Urban Areas. https://doi.org/10.2760/67415.
Scott, A.A., Waugh, D.W., Zaitchik, B.F., 2018. Reduced Urban Heat Island intensity under warmer conditions. Environ. Res. Lett. https://doi.org/10.1088/1748-9326/aabd6c.
Sera, F., Armstrong, B., Tobias, A., Vicedo-Cabrera, A.M., Åström, C., Bell, M.L., Chen, B. Y., De Sousa Zanotti Stagliorio Coelho, M., Correa, P.M., Cruz, J.C., Dang, T.N., Hurtado-Diaz, M., Do Van, D., Forsberg, B., Guo, Y.L.Y., Guo, Y.L.Y., Hashizume, M., Honda, Y., Iñiguez, C., Jaakkola, J.J.K., Kan, H., Kim, H., Lavigne, E., Michelozzi, P., Ortega, N.V., Osorio, S., Pascal, M., Ragettli, M.S., Ryti, N.R.I., Saldiva, P.H.N., Schwartz, J., Scortichini, M., Seposo, X., Tong, S., Zanobetti, A., Gasparrini, A., 2019. How urban characteristics affect vulnerability to heat and cold: a multi-country analysis. Int. J. Epidemiol. https://doi.org/10.1093/ije/dyz008.
Sherwood, S.C., Huber, M., 2010. An adaptability limit to climate change due to heat stress. Proc. Natl. Acad. Sci. U. S. A. https://doi.org/10.1073/pnas.0913352107.
Song, Y., Achberger, C., Linderholm, H.W., 2011. Rain-season trends in precipitation and their effect in different climate regions of China during 1961–2008. Environ. Res. Lett. https://doi.org/10.1088/1748-9326/6/3/034025.
Sospedra-Alfonso, R., Melton, J.R., Merryfield, W.J., 2015. Effects of temperature and precipitation on snowpack variability in the Central Rocky Mountains as a function of elevation. Geophys. Res. Lett. 42, 4429–4438. https://doi.org/10.1002/2015GL063898.
State of the world's cities 2008/2009: Harmonious cities, 2012., State of the World's Cities 2008/2009: Harmonious Cities. https://doi.org/10.4324/9781849772624.
Stewart, I.D., 2011. A systematic review and scientific critique of methodology in modern urban heat island literature. Int. J. Climatol. https://doi.org/10.1002/joc.2141.
Tan, J., Zheng, Y., Tang, X., Guo, C., Li, L., Song, G., Zhen, X., Yuan, D., Kalkstein, A.J., Li, F., Chen, H., 2010. The urban heat island and its impact on heat waves and human health in Shanghai. Int. J. Biometeorol. 54, 75–84. https://doi.org/10.1007/s00484-009-0256-x.
Teare, J., Mathee, A., Naicker, N., Swanepoel, C., Kapwata, T., Balakrishna, Y., du Preez, D.J., Millar, D.A., Wright, C.Y., 2020. Dwelling characteristics influence indoor temperature and may pose health threats in LMICs. Ann. Glob. Heal. 86 https://doi.org/10.5334/aogh.2938.
Theil, H., 1992. A Rank-Invariant Method of Linear and Polynomial Regression Analysis. https://doi.org/10.1007/978-94-011-2546-8_20.
Tran, H., Uchihama, D., Ochi, S., Yasuoka, Y., 2006. Assessment with satellite data of the urban heat island effects in Asian mega cities. Int. J. Appl. Earth Obs. Geoinf. https://doi.org/10.1016/j.jag.2005.05.003.
Tzavali, A., Paravantis, J.P., Mihalakakou, G., Fotiadi, A., Stigka, E., 2015. Urban heat island intensity: a literature review. Fresenius Environ. Bull.
Ulpiani, G., 2021. On the linkage between urban heat island and urban pollution island: three-decade literature review towards a conceptual framework. Sci. Total Environ. 751, 141727 https://doi.org/10.1016/j.scitotenv.2020.141727.
United Nations, Department of Economic and Social Affairs, P.D., 2018. The World 's Cities in 2018. World's Cities 2018 - Data Bookl. (ST/ESA/SER.A/417).
USGS, 2009. SRTM Topography. SRTM Doc. 2, 1. http://dds.cr.usgs.gov/srtm/version_1/Documentatio.
Varquez, A.C.G., Kanda, M., 2018. Global urban climatology: a meta-analysis of air temperature trends (1960–2009). npj Clim. Atmos. Sci. https://doi.org/10.1038/s41612-018-0042-8.
Wan, Z., 2013. MODIS Land Surface Temperature Products Users Guide. Santa Barbara.
Wan, Z., Li, Z.L., 2011. MODIS land surface temperature and emissivity. In: Remote Sensing and Digital Image Processing, pp. 563–577. https://doi.org/10.1007/978-1-4419-6749-7_25.
Wang, Jiong, Kuffer, M., Sliuzas, R., Kohli, D., 2019a. The exposure of slums to high temperature: morphology-based local scale thermal patterns. Sci. Total Environ. 650, 1805–1817. https://doi.org/10.1016/j.scitotenv.2018.09.324.
Wang, Jia, Zhou, W., Wang, Jing, 2019b. Time-series analysis reveals intensified urban heat island effects but without significant urban warming. Remote Sens. 11, 2229. https://doi.org/10.3390/rs11192229.
Ward, K., Lauf, S., Kleinschmit, B., Endlicher, W., 2016. Heat waves and urban heat islands in Europe: a review of relevant drivers. Sci. Total Environ. 569–570, 527–539. https://doi.org/10.1016/j.scitotenv.2016.06.119.
Weng, Q., Lu, D., Schubring, J., 2004. Estimation of land surface temperature-vegetation abundance relationship for urban heat island studies. Remote Sens. Environ. https://doi.org/10.1016/j.rse.2003.11.005.

Wu, W., Zhao, S., Zhu, C., Jiang, J., 2015. A comparative study of urban expansion in Beijing, Tianjin and Shijiazhuang over the past three decades. Landsc. Urban Plan. 134, 93–106. https://doi.org/10.1016/j.landurbplan.2014.10.010.

Xu, R., Liu, J., Xu, J., 2018. Extraction of high-precision urban impervious surfaces from Sentinel-2 multispectral imagery via modified linear spectral mixture analysis. Sensors 18, 2873. https://doi.org/10.3390/s18092873.

Yang, Q., Huang, X., Tang, Q., 2019. The footprint of urban heat island effect in 302 Chinese cities: temporal trends and associated factors. Sci. Total Environ. https://doi.org/10.1016/j.scitotenv.2018.11.171.

Yang, Q., Huang, X., Yang, J., Liu, Y., 2021. The relationship between land surface temperature and artificial impervious surface fraction in 682 global cities: spatiotemporal variations and drivers. Environ. Res. Lett. 16, 024032 https://doi.org/10.1088/1748-9326/abdaed.

Yao, R., Wang, L., Huang, X., Gong, W., Xia, X., 2019. Greening in Rural Areas Increases the Surface Urban Heat Island Intensity. Geophys. Res. Lett. 46, 2204–2212. https://doi.org/10.1029/2018GL081816.

Yao, R., Wang, Lunche, Wang, S., Wang, Lizhe, Wei, J., Li, J., Yu, D., 2020. A detailed comparison of MYD11 and MYD21 land surface temperature products in mainland China. Int. J. Digit. Earth 13, 1391–1407. https://doi.org/10.1080/17538947.2019.1711211.

Zhao, L., Lee, X., Smith, R.B., Oleson, K., 2014. Strong contributions of local background climate to urban heat islands. Nature. https://doi.org/10.1038/nature13462.

Zhao, L., Oleson, K., Bou-Zeid, E., Krayenhoff, E.S., Bray, A., Zhu, Q., Zheng, Z., Chen, C., Oppenheimer, M., 2021. Global multi-model projections of local urban climates. Nat. Clim. Chang. 11, 152–157. https://doi.org/10.1038/s41558-020-00958-8.

Zhao, L., Oppenheimer, M., Zhu, Q., Baldwin, J.W., Ebi, K.L., Bou-Zeid, E., Guan, K., Liu, X., 2018. Interactions between urban heat islands and heat waves. Environ. Res. Lett. 13, 034003 https://doi.org/10.1088/1748-9326/aa9f73.

Zhao, Q., Zhu, Z., Zeng, H., Zhao, W., Myneni, R.B., 2020. Future greening of the Earth may not be as large as previously predicted. Agric. For. Meteorol. 292–293, 108111 https://doi.org/10.1016/j.agrformet.2020.108111.

Zhao, S., Zhou, D., Liu, S., 2016. Data concurrency is required for estimating urban heat island intensity. Environ. Pollut. 208, 118–124. https://doi.org/10.1016/j.envpol.2015.07.037.

Zhou, B., Rybski, D., Kropp, J.P., 2017. The role of city size and urban form in the surface urban heat island. Sci. Rep. https://doi.org/10.1038/s41598-017-04242-2.

Zhou, D., Xiao, J., Bonafoni, S., Berger, C., Deilami, K., Zhou, Y., Frolking, S., Yao, R., Qiao, Z., Sobrino, J.A., 2019. Satellite remote sensing of surface urban heat islands: progress, challenges, and perspectives. Remote Sens. https://doi.org/10.3390/rs11010048.

Zhou, D., Zhao, S., Liu, S., Zhang, L., Zhu, C., 2014. Surface urban heat island in China's 32 major cities: spatial patterns and drivers. Remote Sens. Environ. https://doi.org/10.1016/j.rse.2014.05.017.